Ocean Engineering
January 2023, Volume 268 Pages 113458 (10p.)
https://doi.org/10.1016/j.oceaneng.2022.113458
https://archimer.ifremer.fr/doc/00813/92493/

Induction study of a horizontal axis tidal turbine: Analytical models compared with experimental results

Jouenne Lucien [1], Druault Philippe [1,*], Krawczynski Jean-François [1], Germain Gregory [2]

[1] Sorbonne Université, CNRS, Institut Jean Le Rond d'Alembert, F-75005 Paris, France
[2] Ifremer, Marine Structure Laboratory, 150 quai Gambetta, 62200, Boulogne-sur-mer, France

* Corresponding author : Philippe Druault, email address : philippe.druault@sorbonne-universite.fr

Abstract :

In a water channel, a scale horizontal axis tidal turbine is positioned in a low-disturbance uniform flow, and Particle Image Velocimetry (PIV) measurements are used to investigate turbulent-flow modifications in front of the turbine. The results confirm that even if the axial velocity deficit is mainly governed by the turbine rotational speed, a similar velocity profile is observed regardless of the rotational speed: the uniform flow evolves to a shear flow with a peak velocity deficit in front of the hub. The mean radial velocity component is not sensitive to the turbine rotational speed in front of the hub, whereas its amplitude increases near the tip of the blade as the Tip Speed Ratio increases. PIV database is also used to verify the validity of consolidated analytical induction models. Models based on the axial momentum theory, vortex method, and self-similar models exhibit some discrepancies with experimental measurements, especially in front of the hub. This paper proposes a turbine induction model that separately considers the influence of the hub and the rotating blades. The mean flow deficit in front of the operating turbine calculated using this new model is consistent with the experimental measurements.

Highlights

► Evaluation of the turbine induction effects from the analysis of PIV measurements in a water channel. ► Analysis of the turbine's blockage effects from various turbine thrust values. ► Comparative analysis between experimental database and consolidated analytical turbine induction models. ► Development of a hybrid analytical induction model considering separately the action of the hub and the rotating blades. ► Observation of a good agreement between the proposed model and experimental measurements regardless of the turbine rotational speed.

Keywords : Turbine induction, Turbulence, Analytical induction model

1. Introduction

Structural fatigue of kinetic energy conversion devices is widely recognized to depend on the nature of the incoming flow and its associated variability. Therefore, knowledge of the turbulent flow that affects a turbine is critical to the life span of wind and tidal energy projects. This flow differs from that of free flow because the thrust force of the turbine results in a decrease in the upstream flow in front of the operating turbine. This area is called the induction

or blockage area of the turbine. Thereby, the dynamic pressure increases and modulates the structural load and the rotor efficiency.

Understanding the flow modifications in the immediate vicinity of the rotor is of importance not only for structural reliability, but also for the development of analytical induction models. However, contrary to turbine wake flow analyzes, only a limited number of experimental and numerical studies have been devoted to such an investigation.

From an analytical point of view, a simple expression of the mean axial velocity deficit along the rotor axis can be determined from the axial momentum theory (Glauert, 1935) or from the symmetric vortex theory (Joukowsky, 1912) (also called actuator disk theory):

$$\overline{U}(x) = U_\infty \left[1 - a\left(1 + \frac{x}{\sqrt{R^2 + x^2}}\right)\right] \tag{1}$$

where U_∞ is the far-free upstream mean velocity, a is the axial induction factor, x the upstream axial coordinate, and R the radius of the rotor. Other turbine induction models have also been developed, such as the vortex cylinder model (Branlard and Gaunaa, 2015; Branlard and Meyer Forsting, 2020) and the self-similar model (Troldborg and Meyer Forsting, 2017). Recent studies have made great advances, especially to account for the wind-farm blockage (Branlard and Meyer Forsting, 2020; Segalini, 2021). Note that these models allow only for the representation of the mean velocity field without regard to the turbulence effect. As the need to model the blockage effect associated with a hub cone to better represent the wake of the hub was highlighted, analytical models were developed recently to distinguish between the reduction in velocity due to the rotating blades and the reduction due to the hub (Bontempo and Manna, 2019; Anderson et al., 2020). The rapid distortion theory was also recently used to analyze the flow modifications in front of an actuator disk model corresponding to a rotating turbine (Milne and Graham, 2019).

From a numerical point of view, very few Computational Fluid Dynamics (CFD) studies focused on the analysis of solid turbine blockage. Using high-fidelity CFD methods to accurately simulate realistic unstable turbine loads under turbulent flow conditions was out of reach for some time due to the need to address the range of spatio-temporal scales involved (Van Kuik et al., 2016; Adcok et al., 2020). In order to investigate the mean velocity field in the wind turbine induction area, Reynolds-averaged Navier-Stokes (RANS) simulations (Meyer Forsting et al., 2016) and Large Eddy Simulations (LES) using the actuator line method Meyer Forsting et al. (2018) were carried out.

From an experimental point of view, access to in situ flow description in the wind turbine induction zones was made possible using Lidar or super-large-scale particle image velocimetry (PIV) measurements in selected vertical planes near the turbine (Simley et al., 2016; Howard and Guala, 2015; Slinger et al., 2020; Li et al., 2020). Simley et al. (2016) characterized the mean velocity deficit upstream of the rotor as a function of the thrust coefficient (the turbine induction factor). They also showed an increase in the radial velocity component at the blade tip as the flow accelerates around the turbine. Differences are highlighted

compared to the analytical prediction (Eq. 1), especially for locations close to the rotor plane (Simley et al., 2016; Li et al., 2020). To the authors' knowledge, similar planar in situ measurements in the tidal environment flow have not yet been performed.

Laboratory scale experiments in a wind tunnel or a water channel were also carried out to study the change in flow in front of a turbine (Medici et al., 2011; Chen and Liou, 2011; Howard and Guala, 2015; Bastankhah and Porte-Agel, 2017; Kolekar et al., 2019; Druault and Germain, 2022). The most important modifications of the turbulent velocity field were observed when the incoming flow was uniform (Druault and Germain, 2022) as it turned into a mean shear flow near the rotor. In this case, the blockage effect altered the flow intermittency, resulting in non-Gaussian fluctuations. In contrast, in the presence of an incoming mean shear flow containing large-scale flow structures, it was observed that the turbine did not significantly modify the intermittency of the upstream flow and the large-scale flow structures were relatively unaffected by the rotating blade (Druault and Germain, 2022). This recent result confirmed previous work in which large-scale low-frequency flow structures were not noticeably affected in the induction area (Mann et al., 2018; Kidambi Sekar et al., 2021). Furthermore, these tunnel or channel experimental studies allowed the investigation of the mean axial flow deficit along the rotor axis, and the results were compared to the analytical expression (Eq. 1) (Medici et al., 2011; Bastankhah and Porte-Agel, 2017).

In the present work, the available experimental database (Ikhennicheu, 2019; Magnier et al., 2021; Druault and Germain, 2022) is used to investigate changes in turbulent flow characteristics in front of a scaled turbine with low disturbance uniform flow. Performing experiments in a current-circulating flume tank is advantageous compared to in situ measurements, as it is possible to measure velocities with or without a rotor under various turbine operating conditions. The purpose of this work is twofold: i) to improve our knowledge of turbulent flow modifications upstream a scale tidal turbine operating at different Tip Speed Ratios (TSR), that is, different turbine thrusts; ii) to check the validity of consolidated analytical induction models in the immediate vicinity of the tidal turbine, by comparing the model predictions with the measured mean velocity field under various turbine thrust conditions.

After a short description of the experimental set-up, the velocity measurement method and the test conditions (section 2), the flow modifications upstream the turbine operating at various TSRs are analyzed by successively investigating the first- to fourth-order velocity statistics (section 3). Then, in section 4, an analytical hybrid model is proposed and evaluated from a comparison with the experimental results.

2. Experimental set-up and measurement method

A description of the experimental set-up, the measurement method, and the associated measurement errors are given in (Ikhennicheu, 2019; Ikhennicheu et al., 2019a; Magnier et al., 2020, 2021; Martinez et al., 2021; Druault and

Germain, 2022). Two experimental databases are also available (Ikhennicheu et al., 2019c,d). It is briefly described here for the completeness of this article.

Experiments are carried out in the IFREMER (French Institute for the Exploitation of the Sea) wave and current circulation flume tank whose dimensions are indicated in Fig. 1. All experiments are carried out with a constant far upstream velocity $U_\infty = 1\,\mathrm{m\,s^{-1}}$ with a low turbulence intensity $I_\infty = 1.5\%$. An hydrodynamically smooth wall boundary layer (Ikhennicheu et al., 2019b; Ikhennicheu, 2019) is developed over the wall. To reproduce realistic flow conditions that can occur at a potential French water site, the Alderney race (Sentchev et al., 2020; Ikhennicheu, 2019), the far upstream flow interacts with a wall-mounted cube of side $H = 0.25\,\mathrm{m}$ followed $2H$ downstream with a wall-mounted square cylinder of height H and $6H$ long. The obstacles are placed in the center of the test section, symmetrically around the span-wise origin $y = 0$. Note that H will be used later to normalize the spatial variables. The Reynolds number $Re = U_\infty H/\nu$ (with ν the water kinematic viscosity) is around 2.5×10^5, which is close to the real conditions in situ (Ikhennicheu et al., 2019b; Magnier et al., 2021).

A 1:20 scaled tri-bladed horizontal axis tidal turbine is successively positioned at two streamwise locations ($x^* = x/H = 10, 16$) in the obstacle wake. The origin of the x axis corresponds to the x center of the cylinder. The turbine has a diameter $D = 0.724\,\mathrm{m}$ and its center is located mid-depth ($z = 4H$) and mid-span ($y = 0$) in the tank (see Fig. 1). The turbine rotational speed is controlled and the blade pitch does not change. The turbine characteristics are provided in (Gaurier et al., 2017, 2020a; Druault et al., 2022).

In this study, the turbine is considered parked (denoted TSR0) or rotating. The nominal operating point, which corresponds to the largest bending moments, is obtained when the Tip Speed Ratio, $TSR = \omega R/U_\infty$, is 4 (Magnier et al., 2020) with $R = D/2$ and ω is the angular rotational speed. The following TSRs $(3, 4, 5)$ are successively considered in the present work. Each root of the blade is equipped to allow measurements of the two forces (T_x, T_y) along the respective axes. The global thrust of the turbine T_t and torque M_t applied on the main rotational axis are also measured.

To characterize the 2D flow upstream of the turbine at the height of the rotor axis ($z^* = 4$), Laser Doppler Velocimetry (LDV) measurements are performed (Gaurier et al., 2020a; Druault and Germain, 2022). A reference mean axial velocity outside the turbine induction area is then estimated and used to evaluate the turbine performance parameters.

In order to characterize the turbine induction area, planar Particle Image Velocimetry (PIV) measurements are performed to access instantaneously the axial (u) and vertical (w) velocity components in a vertical plane located at $y = 0$ in front of the turbine (see Fig. 2). As the turbine is located at mid-depth of the tank so relatively close to the triangular form of the PIV laser sheet (Gaurier et al. (2020b), figure 4), the vertical PIV plane is in consequence reduced by the lens aperture, due to the shadow effect. Consequently, instantaneous velocity components extracted along a vertical line at $0.07D = 0.05\mathrm{m}$ upstream of the extremity of the hub are only retained for analysis. The velocity vectors are then

available for the $N_z = 74$ points that sweep the vertical line $z^* \in [2.53 : 5.44]$. $N_t = 2700$ instantaneous vector fields sampled at $dt = 0.067\,\mathrm{s}$ (the PIV sampling frequency is 15Hz) are obtained. In the present work, we focus on turbulent flow modifications in the turbine blockage area under uniform conditions. Then, we choose to exploit the velocity fields extracted only at the upper part of the vertical z-line, $z^* \in [4 : 5.44]$. In fact, in this area, the mean flow is uniform and homogeneous along the spanwise direction while below $z^* < 3$, the wake mean flow presents a slight mean axial velocity z-gradient (Magnier et al., 2021; Druault and Germain, 2022).

For every axial turbine position ($x^* = 10, 16$), five configurations are examined: without a turbine (free flow), with a parked turbine, and with a rotating turbine for three TSR values. The following associated notations will be used for the rest of the paper: free, TSR0, TSR3, TSR4 and TSR5, respectively. For each configuration, the velocity vector fields are measured simultaneously with the turbine forces with a sampling frequency of 15Hz and 120Hz, respectively. Note that for the TSR0 case, one blade is exactly at the top dead center ($y = 0$), which corresponds to the vertical position of PIV line measurements. Previous investigations obtained with the same turbine as ours and in the same experimental set-up, but with an upstream homogeneous turbulent flow with a turbulence intensity of 13% showed that the mean velocity remains unchanged up to 1D along the hub axis (Deskos et al., 2020).

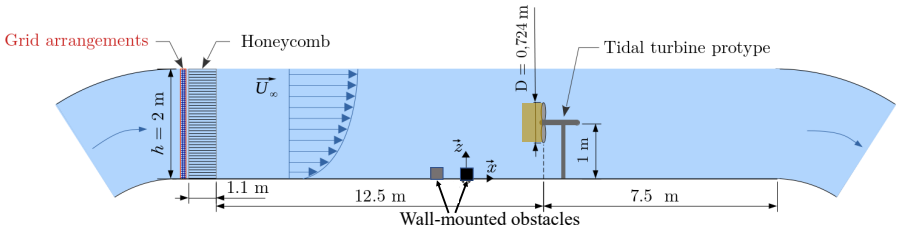

Figure 1: Schematic view of the experimental setup including the wall-mounted obstacles and the PIV measurement plane (orange color) in front of the operating turbine.

3. TSR effect on the flow modification in front of the turbine

The purpose of the present section is to analyze the flow modifications in front of the operating turbine as a function of the thrust of the turbine. We then successively analyze the first- to fourth- order velocity moments along the vertical line in front of the turbine for the two turbine x-locations, $x^* = 10, 16$. The velocity statistics are deduced from the Reynolds decomposition as for the axial velocity component:

$$u(z,t) = \overline{U}(z) + u'(z,t) \tag{2}$$

where an overbar denotes the time average operator and u' is the component of the fluctuating velocity. The statistics obtained for various TSR (that is,

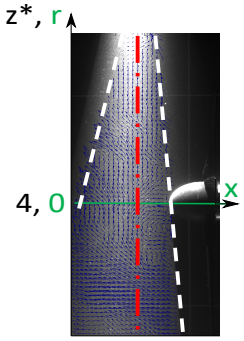

Figure 2: Illustration of an instantaneous PIV velocity vector field and the location of the vertical line under consideration (red line) where instantaneous velocity vectors are extracted. (x, z^*) cartesian coordinate system and (x, r) cylindrical one are indicated. Dashed white lines indicate the reduction of PIV measurements plane due to the triangular laser sheet.

for various turbine thrusts) will be compared among themselves and with those computed from the cases free and TSR0.

3.1. Turbine performance parameters

Before examining the effect of the turbine thrust on the turbine blockage, the following thrust and power parameters are examined:

$$C_T = \frac{\overline{T}}{\frac{1}{2}\rho A \overline{U_{LDV}}^2} \quad \text{and} \quad C_P = \frac{\overline{M}\omega}{\frac{1}{2}\rho A \overline{U_{LDV}}^3} \tag{3}$$

where $\overline{U_{LDV}}$ is the reference LDV mean axial velocity component, $A = \pi R^2$ is the rotor swept area, $\rho = 1000\,\mathrm{kg/m^3}$ is the water density, $\overline{T}$ and $\overline{M}$ are the time average thrust and torque of the turbine, respectively. $\overline{U_{LDV}}$ is $1.07\,\mathrm{m\,s^{-1}}$ and $1.03\,\mathrm{m\,s^{-1}}$ for $x^* = 10$ and $x^* = 16$, respectively. Two values are retained for $\overline{T}$: 1) the total turbine thrust $\overline{T_t}$ and 2) the sum of the blade thrust $\overline{T_b} = \overline{\sum_{i=1}^{3} T_x^i}$, without taking into account the thrust of the hub. The coefficients C_{T_t} and C_{T_b} are then calculated with the associated sweeping area A and A_b, respectively, where A_b corresponds to the rotor area subtracted from the hub area. The time average of these coefficients is also determined based only on the thrust moments and signals for which the blade lies in the upper part of the rotor ($z^* > 4$). A less than 1% difference is obtained with the time average computed with all available instants. The slight mean axial velocity shear observed for $z^* < 3$ does not have a real incidence on these time-average coefficients. The thrust coefficients and their associated standard-deviations σ are indicated in table 1. The time duration for each blade thrust signal is long enough to ensure the statistical convergence of the associated average and standard deviation estimates, which show similar values for each blade thrust signal.

	$x^* = 10$				$x^* = 16$			
	TSR0	TSR3	TSR4	TSR5	TSR0	TSR3	TSR4	TSR5
C_{T_t}	0.18	0.65	0.83	0.91	0.17	0.70	0.90	0.98
$\sigma_{C_{T_t}}$	0.010	0.014	0.022	0.025	0.020	0.016	0.024	0.032
C_{T_b}	0.15	0.60	0.77	0.85	0.15	0.65	0.85	0.92
$\sigma_{C_{T_b}}$	0.008	0.012	0.021	0.024	0.017	0.015	0.023	0.030
C_P	0	0.34	0.4	0.38	0	0.37	0.43	0.40
σ_{C_P}	0	0.012	0.021	0.022	0	0.014	0.022	0.027
a	0.05	0.21	0.3	0.35	0.04	0.23	0.34	0.42

Table 1: Comparison of the turbine performance parameters and their associated standard deviation σ determined for each flow configuration (TSR0, TSR3, TSR4 and TSR5) at both turbine locations ($x^* = 10, 16$). The axial induction factor $a = 0.5\left(1 - \sqrt{1 - C_T}\right)$ is also indicated.

The highest C_p values are obtained, as expected (Magnier et al., 2020), for the TSR4 case that corresponds to the nominal operating point. The C_T and C_p coefficients follow similar tendencies with respect to the TSR as those obtained previously in the same circulation basin with other turbulent incoming flow conditions (Mycek et al., 2014a,b; Gaurier et al., 2020b). Both performance coefficients increase slightly as the turbine goes upstream. In addition, an increase in the TSR increases fluctuations in both the turbine thrust and torque signals, especially between the cases TSR3 and TSR4. In contrast, similar standard deviation values related to the coefficients C_T and C_p are obtained for TSR4 and TSR5. These results agree with those previously obtained (Mycek et al., 2014a; Blackmore et al., 2016).

The comparison of C_{T_t} and C_{T_b} highlights that the thrust of the hub remains the same regardless of the TSR. The hub thrust is mainly derived from the drag characteristics of the ellipsoidal hub while the thrust of the blades is derived from the airfoil's lift and drag characteristics. To the authors' knowledge, no similar results were reported. Ishihara and Qian (2018) numerically investigated the wind turbine wake in which different thrust coefficients are considered. Whatever the turbine thrust values are, they always considered that the hub loss is constant (see equation 17 in their paper) suggesting that the hub thrust is independent of the turbine thrust. Similarly, Ebdon (2019) observed that whatever the TSR is, the stanchion thrust is similar in each case. By analogy with these studies and considering the hub as a bluff body, we can state that the thrust of the hub remains constant for the present turbine operational points, TSR $\in [3:5]$.

When considering the local blade thrust values (see Table 2), the blade thrust is higher when the blades rotate compared to the one in front of a fixed blade (TSR0). This is due to the three-dimensional effect. During zero yaw operation, blade rotation imposes additional flow resistance due to the Coriolis and centrifugal forces (Schreck and Robinson, 2022; Bangga et al., 2017), thus significantly increasing blade thrust.

	$x^* = 10$				$x^* = 16$			
	TSR0	TSR3	TSR4	TSR5	TSR0	TSR3	TSR4	TSR5
$\overline{T_t}$	38.6	152.5	194.1	214.2	37.0	146.6	178.0	196.9
$\overline{T_x^1}$	11.0	46.3	59.6	66.1	11.2	45.0	55,0	61,0
$\overline{T_x^2}$	10.4	46.0	60.5	67.6	10.3	45.1	56.2	62.8
$\overline{T_x^3}$	10.6	46.04	58.9	64.9	10.4	45.0	54.5	60.0

Table 2: Values for blade and turbine thrust for each studied configuration.

3.2. Mean velocity modifications

The first order statistics of the velocity fields extracted along the vertical z-line, $z^* \in [4 : 5.44]$ are determined. Note that the z-extend of the measurement line corresponds to the upper radius part of the rotor (see Fig. 2). In this sense, instead of using the z variable, the radial r spatial variable will be used for the rest of the paper, allowing an easier comparison with the analytical induction model (see section 4). The position $r = 0$ corresponds to the height $z^* = 4$. Thus, along the measurement line, the measured vertical velocity component w corresponds to the radial velocity component u_r (in polar coordinates).
Under this experimental set-up, the mean flow without a turbine is uniform with $\overline{U_{free}} = 0.98\,\mathrm{m\,s^{-1}}$. Figure 3 compares the radial evolution of the mean axial velocity component in front of the turbine with the free flow. In this figure, the normalized velocity deficit (expressed as a percentage):

$$100 \times |\overline{U(r)} - \overline{U_{free}}|/\overline{U_{free}} \tag{4}$$

is also displayed. For both turbine locations, similar behaviors are observed. The uniform mean axial velocity field evolves towards a shear flow in front of the turbine with its minimum value reached at the center of the turbine. This is in agreement with previous experimental results upstream of a wind or tidal turbine (Bastankhah and Porte-Agel, 2017; Howard and Guala, 2015; Medici et al., 2011; Simley et al., 2016; García Regodeseves and Santolaria Morros, 2021; Druault and Germain, 2022). A higher turbine rotational speed results in a higher mean axial velocity deficit (higher blockage) (see Table 3). The comparison between TS3, TSR4 and TSR5 profiles exhibits a non-linear behaviour. This is directly related to the different modes operating at TSR3 and TSR5 as indicated in both table 1 with various values of C_t and in Shoukat et al (2022). At mid-span ($r/R = 0.5$), regardless of the x section, the percentage deficit is 14.1%, 18.7% and 21.5% for TSR3, TSR4 and TSR5, respectively. Simley et al. (2016) performed measurements of the axial mean velocity upstream of a wind turbine with an induction factor of 0.25. In table 4, the velocity deficit observed in the case $x^* = 16$, TSR3 for which the induction factor is 0.23, is similar to the available measurements. The agreement between the two measurements is satisfactory.
Recently, it was observed that for a fixed TSR, the percentage of velocity deficit remains globally the same regardless of the nature of the incoming flow (Druault

and Germain, 2022). The current results confirm that the percentage deficit is primarily governed by the rotational speed of the turbine (Chen and Liou, 2011; Kolekar and Banerjee, 2015). Thus, the deceleration decreases with the thrust coefficient, but the overall shape of the mean axial velocity profiles remains unchanged in the proximity of the rotor.

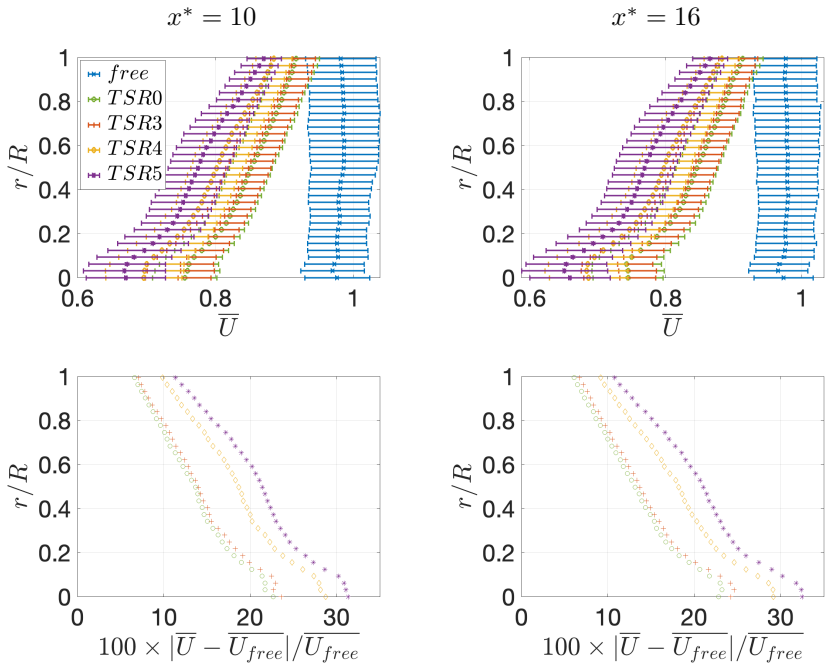

Figure 3: Top: superposition of axial mean velocity profile $\overline{U}$ along r for free (blue), TSR0 (green), TSR3 (red), TSR4 (yellow) and TSR5 (purple). Bottom: normalized velocity deficit expressed in percentage values (see Eq. 5).

	$x^* = 10$				$x^* = 16$			
	TSR0	TSR3	TSR4	TSR5	TSR0	TSR3	TSR4	TSR5
$r = 0$	21.7	22.7	28.1	30.9	22.8	24.2	29.2	32.4
$r = 0.5R$	13.7	14.0	18.7	21.4	13.6	14.1	18.6	21.5
$r = R$	6.2	6.8	9.4	10.7	6.1	6.7	9.2	10.8

Table 3: Comparison of percentage deficit $100 \times |\overline{U} - \overline{U_{free}}|/\overline{U_{free}}$ for TSR0, TSR3, TSR4, TSR5 at $r = 0, R/2, R$.

The blockage effect is greater when the blades rotate, as their rotation amplifies the aerodynamic forces due to the Coriolis and centrifugal forces (Schreck and Robinson, 2022; Bangga et al., 2017). It is interesting to observe that for both turbine x-positions, the axial mean velocity at TSR0 is very close to the axial mean velocity at TSR3. This can be explained by the lower rotational tur-

	$r = 0.25R$	$r = 0.5R$	$r = 0.75R$	$r = R$
(Simley et al., 2016) : $\overline{U}/U_\infty$	0.84	0.85	0.88	0.93
$x^* = 16$, TSR3 : $\overline{U}/U_{free}$	0.83	0.86	0.90	0.93

Table 4: Comparison between previous measurements Simley et al. (2016) and present PIV measurements ($x^* = 16$, TSR3 case).

bine speed in this case, which limits the development of the three-dimensionality of the incoming flow.

Figure 4 shows the superposition of the radial mean velocity component (or vertical component) and its associated percentage deficit calculated as: $100 \times |\overline{U_r} - \overline{U_{r_{free}}}|/\overline{U_{free}}$. Only the results at $x^* = 16$ are presented, similar results are obtained at $x^* = 10$ (see Table 5). In free flow, this mean component is very small in relation to the magnitude of the axial mean velocity, illustrating the uniform flow conditions. The presence of the turbine causes the radial expansion of the flow and the velocity field changes from a uniform to a shear profile, in agreement with previous studies (Medici et al., 2011; Li et al., 2020; Simley et al., 2016; García Regodeseves and Santolaria Morros, 2021; Druault and Germain, 2022). Whatever the TSR case, similar profiles with two distinct regions are visible. First, around the hub, a similar velocity gradient is obtained independently of the rotational speed of the turbine or for the parked turbine. At $r = 0$, the radial mean component is not affected by the turbine rotational speed. Second, near the tip of the blade, the radial distribution of the velocity exhibits a dependency on the TSR. The influence of the TSR is stronger in this area, and a higher turbine rotational speed results in a higher mean radial velocity (see Table 5). This result can be related to previous observations emphasizing that the near-wake region (initiation of the large-scale structures) is significantly influenced by the TSR. This is also directly related to the different peak values for the mean radial velocity observed at $r = R$.

	$x^* = 10$			
	TSR0	TSR3	TSR4	TSR5
$r = 0$	-0.01 (0.6)	-0.01 (0.4)	-0.01 (0.3)	-0.01 (0.8)
$r = 0.5R$	0.03 (5.1)	0.03 (5.6)	0.04 (6.8)	0.04 (7.4)
$r = R$	0.04 (5.7)	0.05 (6.8)	0.08 (10.0)	0.09 (12.2)
	$x^* = 16$			
	TSR0	TSR3	TSR4	TSR5
$r = 0$	-0.03 (0.5)	-0.03 (0.8)	-0.03 (0.5)	-0.03 (0.3)
$r = 0.5R$	0.03 (5.3)	0.03 (5.7)	0.04 (7.0)	0.04 (7.6)
$r = R$	0.04 (5.8)	0.05 (7.0)	0.08 (10.4)	0.09 (12.7)

Table 5: Comparison of the radial mean velocity expressed in $\mathrm{m.s}^{-1}$ and enclosed in parentheses the velocity deficit $100 \times |\overline{U_r} - \overline{U_{r_{free}}}|/\overline{U_{free}}$ for each flow configuration, at selected radial locations: $r = 0$, $r = R/2$ and $r = R$.

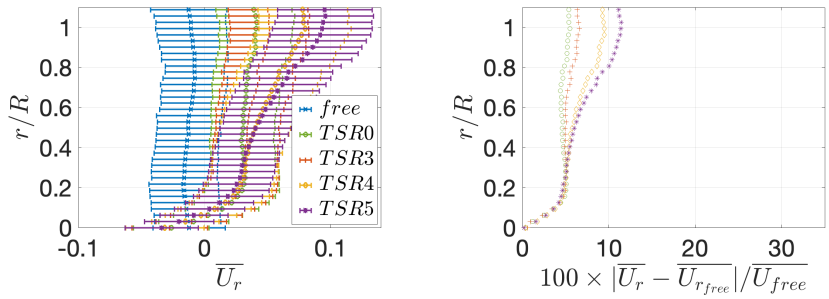

Figure 4: Left: Superposition of radial mean velocity profiles $\overline{U_r}$ along r for free (blue), TSR0 (green), TSR3 (red), TSR4 (yellow) and TSR5 (purple). Right: Corresponding percentage velocity deficit.

3.3. Modifications of the second order velocity statistics close to the operating turbine

The radial distribution of the Reynolds tensor components, $\overline{u'^2}$ and $\overline{u_r'^2}$ is shown in Fig. 5. For the present uniform incoming conditions with low turbulence intensity, the second-order velocity statistics have very low amplitudes, but some tendencies emerge. In front of the hub ($r/R < 0.2$), the $\overline{u'^2}$ magnitude increases by comparison with the magnitude of the free flow configuration. This is a consequence of the strong gradients of the mean axial flow along the radial direction. As r increases, the levels of $\overline{u'^2}$ decrease to converge at $r = R$ toward approximately half the level observed for the free flow regardless of the TSR. This result could be related to previous work (Hancock and Pascheke, 2014) in which a decrease in turbulence intensity was reported just behind the turbine and was explained as a possible consequence of the decrease in turbulence intensity upstream of the turbine due to blockage effect.
For $r < R/2$, the amplitude of $\overline{u_r'^2}$ remains similar to that of free flow regardless of the test cases. On the contrary, the dependence on TSR is clearly seen in the upper part of the blade, where an increase in TSR leads to an increase in the level of $\overline{u_r'^2}$. This is related to previous observations of the modification of the radial mean velocity at the tip of the blade. The present results appear to indicate a redistribution of the kinetic energy near the rotor due to the turbine rotational speed. An analysis of all the Reynolds tensor components, especially the angular component $\overline{u_\theta'^2}$, is necessary to confirm this statement.

The Discrete Fourier Transform is now applied to the fluctuating u' signal which is split into blocks of 1024 samples with overlapping of 50%. The velocity spectrum is then averaged over blocks and a smoothing technique is finally applied to it (Druault and Germain, 2022). Fig. 6 represents the u'-spectra as a function of the frequency and computed at three radial positions: $r = 0$, $r = R/2$ and $r = R$, for the free, TSR3, TSR4 and TSR5 cases. In each radial position, the velocity spectra are of low amplitude, and those computed at TSR3, TSR4 and TSR5 are comparable regardless of the radial position. As

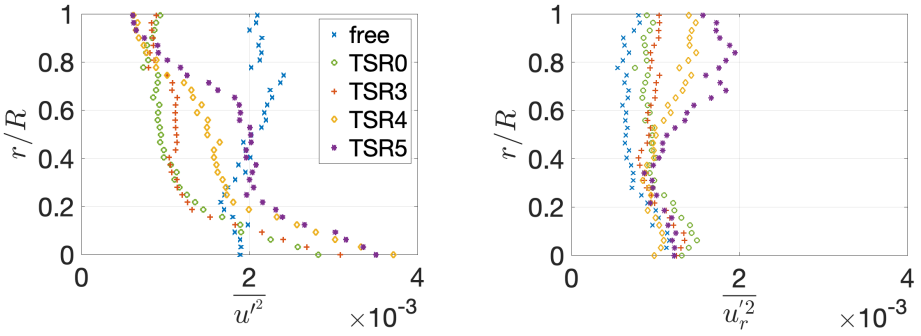

Figure 5: Superposition of $\overline{u'^2}$ (left) and $\overline{u_r'^2}$ (left) for the free, TSR0, TSR3, TSR4 and TSR5 cases. (turbine located at $x^* = 16$).

previously noted (Deskos et al., 2020) the rapid distortion theory shows that two dominant effects act in front of an actuator disk model: one being blockage and the other being turbulence distortion. Even if no more measurements are presently available at other upstream locations, the comparison with the free flow database makes possible a preliminary analysis of the distortion-blockage effects. Thus, along the rotor axis ($r = 0$), an attenuation of the low-frequency spectral velocity component seems to be observed when the turbine rotates while an opposite effect is obtained in front of the rotating blades ($r = R/2$ and $r = R$). Present measurements in the close proximity of the rotating turbine are certainly not sufficient to accurately analyze the relative of the blockage-distortion effects. However, these preliminary results emphasize the need to take into account separately the hub blockage and the rotating blade effects which act differently.

3.4. Intermittency

To further characterize the impact of the blockage effect induced by the presence of a turbine in the modifications of a homogeneous incoming turbulent flow, we choose to assess higher-order moments of the axial velocity component. The third- and fourth-order moments of the axial velocity component, namely the skewness and flatness coefficients, respectively, are calculated as $S_u = m_3 m_2^{-3/2}$ and $F_u = m_4 m_2^{-2}$, where $m_j = {N_t}^{-1} \sum_{i=1}^{N_t} [u'(i)]^j$ is the jth moment about the mean. The radial distribution of the skewness and flatness of the axial velocity component is shown in Fig. 7.

Higher-order moments appear to be sensitive to the presence of the turbine, as seen in the transition from a positively skewed distribution in the absence of the turbine to a negatively skewed distribution for the cases where the turbine is present.

The radial distribution of the flatness exhibits larger values in the presence of the turbine than those observed in the free case, except near the hub where the blockage effect prevents one from forming any clear conclusion about the

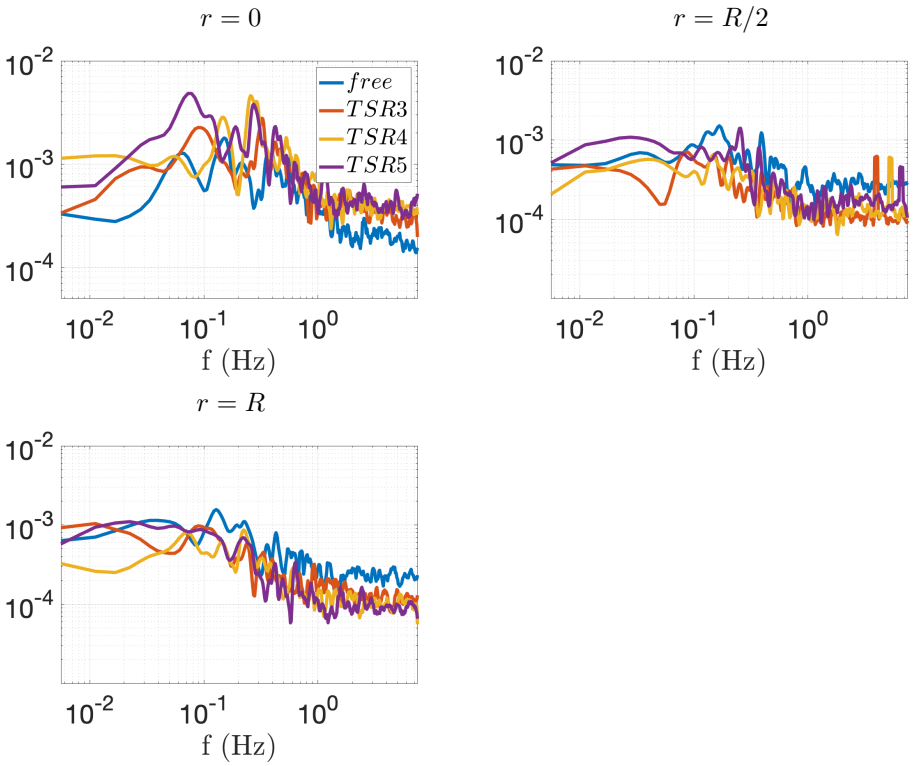

Figure 6: Superposition of the velocity PSD for the free, TSR3, TSR4 and TSR5 cases (turbine located at $x^* = 16$).

statistical nature of the fluctuations. Still, far enough from the hub ($r/R > 0.2$) a collective behavior is noticeable, as the flatness appears to converge towards approximately the same levels for all the different TSRs, with larger values than in the free case, indicative of a probability distribution with predominance of large tails (large-magnitude u values).

4. Comparative analyses between mean flow measurements and analytical induction models

A description of the main induction models available and tested in the wind turbine industry was recently reported in (Branlard et al., 2020). In this section, a brief description of the selected models is given. As these models do not necessarily distinguish the blockage effects related to the hub cone and the rotating blades, a specific model associated with the hub blockage is also presented. The validity of these models is assessed by comparing their velocity predictions with the experimental measurements performed in front of the turbine, which are detailed in the previous section.

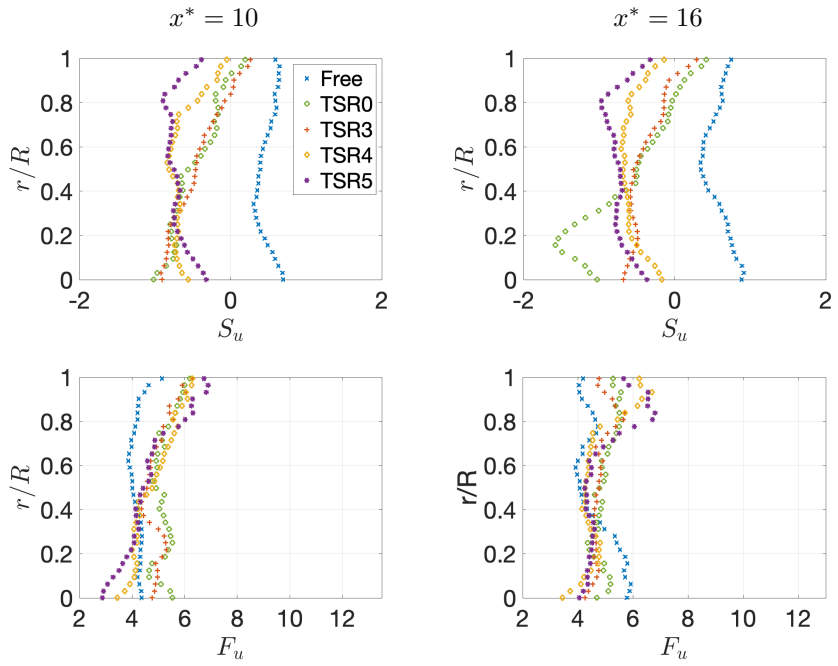

Figure 7: Superposition of the skewness (top) and flatness (bottom) coefficients of the axial velocity component along r for free (blue), TSR0 (green), TSR3 (red), TSR4 (yellow) and TSR5 (purple) for both turbine's locations.

4.1. Analytical induction models

Briefly, a uniform axial flow with velocity U_∞ is assumed to interact with an actuator disk of surface S (rotor representation), with constant thrust T. In this case, the thrust coefficient C_T is equal to $4a(1-a)$ with a the induction factor related to the velocity deficit $a = (U_\infty - U_R)/U_\infty$ and U_R the axial velocity in the rotor plane.

A first analytical expression of the axial (mean) velocity along the rotor axis is written using the Vortex Sheet (VS) theory or the one-dimensional axial momentum theory (Sorensen, 2016):

$$\frac{\overline{U}}{U_\infty}(x) = 1 - a\left[1 + \frac{x}{R}\left(1 + \left(\frac{x}{R}\right)^2\right)^{-\frac{1}{2}}\right] \tag{5}$$

with x the negative axial coordinate upwind of the rotor. Numerous experimental and numerical databases (wind or tidal turbine) have verified the validity of this simplified expression. Various degrees of success were found, especially in the proximity of the rotor.

The Vortex Cylinder (VC) induction model proposed by Branlard and Gaunaa (2015) is based on the symmetric vortex theory (Joukowsky, 1912). The denoted

vortex system (Branlard and Gaunaa, 2015) is used to model a rotor with an infinite number of blades. A single vortex cylinder is considered with constant circulation related to a constant thrust coefficient as follows:

$$\gamma_t = -U_\infty(1 - \sqrt{1 - C_T}) \tag{6}$$

Then the axial velocity component is calculated by integrating the Biot-Savart law, for $r \neq R$ (Branlard and Gaunaa, 2015; Branlard and Meyer Forsting, 2020):

$$U_{VC}(x,r) = \frac{\gamma_t}{2}\left[\frac{R-r+|R-r|}{2|R-r|} + \frac{xk(x)}{2\pi\sqrt{rR}}\left(K(k^2(x)) + \frac{R-r}{R+r}\Pi(k^2(0),k^2(x))\right)\right] \tag{7}$$

with $k(x,r) = 4rR/((R+r)^2+x^2)$ and $K(k^2(x))$, $\Pi(k^2(0),k^2(x))$ the elliptic integrals of the first and third kind. The mean axial velocity is calculated by adding U_∞:

$$\overline{U}(x,r) = U_\infty + U_{VC}(x,r) \tag{8}$$

The Self-Similar (SS) model developed by Troldborg and Meyer Forsting (2017) is initially based on the self-similar solution of a plane jet. By performing more than 100 RANS simulations coupled with an actuator disk approach, the authors found that far upstream of the porous disk ($x < -R$) the axial velocity is self-similar and independent of the rotor geometry. They then found the following expression derived from the results of their numerical simulations (Troldborg and Meyer Forsting, 2017):

$$\overline{U}(x,r) = U_\infty + U_{SS}(x,r) \tag{9}$$

with

$$U_{SS}(x,r) = \frac{\gamma_t/2(1+\frac{x}{\sqrt{x^2+R^2}})}{cosh^\alpha(\frac{\beta r}{r_m(x)})} \text{ with } r_m(x) = R\sqrt{\lambda(\eta + \frac{x^2}{R^2})} \tag{10}$$

with γ_t defined in Eq. 6, $\beta = \sqrt{2}$, $\alpha = \frac{8}{9}$, $\lambda = 0.587$ and $\eta = 1.32$.

The VC and SS models are implemented using the source codes available in Branlard (2017). Both the VC and SS models do not distinguish between the hub blockage and the blockage related to the rotating blades. This can pose a limitation near the turbine because the hub behaves differently than the rotating blade. To take into account the hub induction effect (or the nacelle blockage effect), Anderson et al. (2020) recently developed an analytical model that calculates the axial velocity upstream and downstream of an ellipsoidal hub. They considered an ellipsoid of eccentricity e and of semi-axes of revolution a_x (along x) and a_r (along r). In semi-elliptic coordinates (μ, ζ) defined in

(Anderson et al., 2020), the potential velocity is given by:

$$\phi(\mu,\zeta) = U_\infty a_x \mu \left[\frac{1}{1-e^2} - \frac{1}{2e} log\frac{1+e}{1-e}\right]^{-1} \left[\frac{1}{2}\zeta log\frac{\zeta+1}{\zeta-1} - 1\right] \tag{11}$$

resulting in the following expression of the axial velocity component:

$$\overline{U}(x,r) = U_\infty + U_{hub}(x,r) = U_\infty + \frac{\partial\phi}{\partial\mu}\frac{\partial\mu}{\partial x} + \frac{\partial\phi}{\partial\xi}\frac{\partial\xi}{\partial x} \tag{12}$$

4.2. New hybrid induction model

As mentioned in the previous section, the models VC and SS, which are based on a uniform thrust coefficient in the porous disk area, do not specifically take into account the effect of the nacelle. In contrast, the velocity deficit in front of the hub is different and actually greater than that upstream of the rotating blades, as evidenced by the results shown in Fig. 3. Then, we propose to combine two models efficiently to better reproduce the mean axial velocity deficit along the radial direction: close to the rotor $r \in [0 : r_c]$, the hub induction model (Eq. 12) is considered using the geometric parameters of the current hub geometry, and for $r \in [r_c : R]$ the *classic* induction model (Eq. 9 for the SS model) is considered. To determine the radial location (r_c) of the connection between these models, we determine $U_{hub}(x,r)$ and investigate the influence of the induction of the hub along the radial direction. For $r \geq 0.45R$, the radial velocity recovers its value at $r = 0$. When regarding the axial $U_{hub}(x,r)$ profile as a function of r at $x = 0.05$m upstream of the hub, this profile recovers the U_∞ value to within three per mill, at $r = 0.45R$. Moreover, experimental measurements (see Fig. 4-left) showed that the radial velocity profile exhibited a change around $r = 0.4R$ as a function of the TSR, which may be related to the rotational action of the blade. Based on these results, the value $r_c = 0.45R$ is retained to connect both models.

Previous models are based on the velocity U_∞ In an attempt to compare the results of the analytical model with the experimental measurements performed in front of the turbine ($x = -0.05$), we choose here the uniform free-flow velocity U_{free} as the reference velocity in the SS model. Furthermore, to account for the effect of turbine thrust, the velocity determined at $r = r_c$ in the model SS is used as the reference velocity for the *hub* model. The hybrid induction model allows for the estimation of the axial velocity as follows (at $x = -0.05$):

$$\begin{cases} r \in [r_c : R],\ \overline{U}(r) = U_{free} + U_{SS}(r) \\ r \in [0 : r_c],\ \ \overline{U}(r) = U_{free} + U_{SS}(r_c) + U_{hub}(r) \end{cases} \tag{13}$$

To further improve this hybrid induction model denoted $SS + hub$ in the rest of the article, the thrust coefficient C_{t_b} associated only with blade thrust (see section 3.1) is used in the SS model.

4.3. Comparative analysis

The models VC, SS, and $SS + hub$ are used to predict the axial mean flow deficit in front of the turbine. Figure 8 compares the velocity estimates for six configurations: TSR3, TSR4, and TSR5 for the two turbine positions. Table 6 indicates the percentage relative error E, compared to the reference PIV database:

$$E_m = 100 \times \frac{\overline{U_m} - \overline{U_{PIV}}}{\overline{U_{PIV}}} \tag{14}$$

with m, the index that stands for the model under consideration. In this table, the radial average $\langle E_m \rangle$ of the associated error is also mentioned for each case.

The vortex sheet model (estimation of axial velocity along the rotor axis, $r = 0$) provides a satisfactory magnitude of the mean axial flow only at high turbine thrust (large TSR values) with around 1% error compared to the experimental data (Table 6). In contrast, for low thrust (TSR3 case) differences appear, which confirm previous comparative results, especially in the vicinity of the hub. On the other hand, the axial velocity value on the hub axis is the same for the models VC and SS. A much better estimate of the axial velocity at $r = 0$ is obtained thanks to the $SS + hub$ model, which allows a better representation of the shape of the axial mean shear around the hub, i.e. for $r < 0.4$.

As r increases, the results of VC deviate from the PIV velocity measurements, especially for $r/R \in [0.4 : 0.6]$. The SS model provides a good trend in the flow deficit ahead of the rotating blades $r/R \in [0.4 : 1]$, although there are some discrepancies near the hub. The best results are provided by the $SS + hub$ model. It allows us to better represent both the induction effect due to the hub and the rotating blades. In fact, this model improves the representation of the velocity deficit for $r/R > 0.4$ by considering the thrust of the blades $\overline{T_b}$ instead of the total thrust T_t (see Table 1).

It is interesting to observe that the rotational speed of the turbine does not affect the results regardless of the location of the turbine ($x^* = 10, 16$). Therefore, the results obtained with the proposed $SS + hub$ model are in excellent agreement with those obtained experimentally, with a difference of less than 1.4% (on average) when the turbine is placed at $x^* = 10$ and less than 4.1% at $x^* = 16$ (see Table 6).

The proposed new $SS + hub$ model provides a very satisfactory representation of the mean axial velocity deficit near the turbine under uniform flow conditions. Globally, the main limitation of the present analytical model concerns the connection between both models that is the determination of r_c which is based here on the change of the radial velocity profile. The parameters of the SS model are exactly the same as the ones provided in the reference article (Troldborg and Meyer Forsting, 2017) and the parameters of the hub model are only based on the hub geometry which could be reasonably accessed.

5. Conclusion

This paper provided new insights into the effects of turbine blockage in a low disturbance uniform flow. The velocity deficit in the vicinity of the rotor

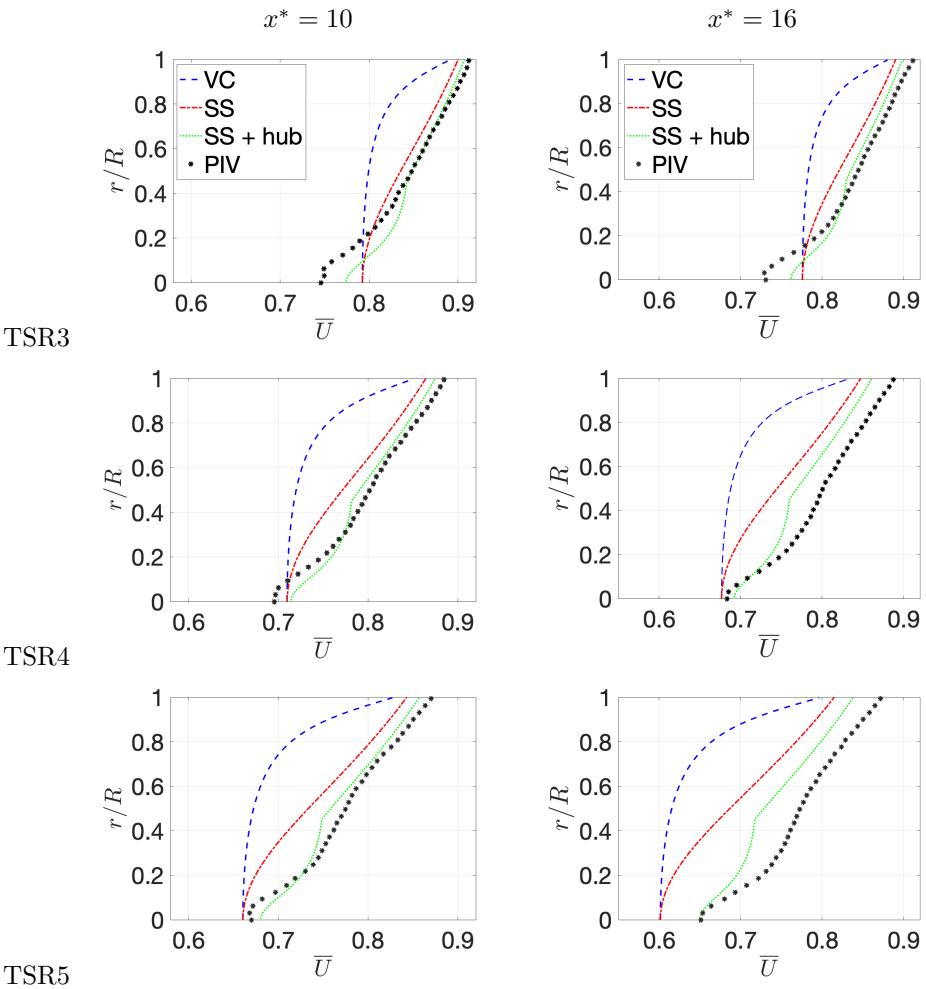

Figure 8: Comparison between the mean axial velocity in front of the turbine ($x = -0.05$) predicted with VC, SS, $SS + hub$ models with PIV measurements for three TSRs, with the turbine's position located at $x^* = 10$ (left column) and at $x^* = 16$ (right column).

	$x^* = 10$			$x^* = 16$		
	TSR3	TSR4	TSR5	TSR3	TSR4	TSR5
$r = 0$						
E_{VS}	8.3	5.1	2.4	7.2	0.7	6.0
$E_{VC/SS}$	6.2	2.0	1.5	5.9	1.5	8.8
E_{SS+hub}	3.8	2.6	1.5	4.0	0.8	1.5
$r = 0.5R$						
E_{VC}	5.7	10.2	13.2	6.8	13.7	20.0
E_{SS}	1.5	3.8	5.3	2.3	6.6	10.7
E_{SS+hub}	0.1	1.4	2.1	0.5	3.4	5.2
$r = R$						
E_{VC}	2.4	3.8	5.0	2.9	5.7	8.0
E_{SS}	1.3	2.3	3.2	1.8	4.0	5.8
E_{SS+hub}	0.6	1.1	1.6	0.9	2.4	3.1
$r \in [0 : R]$						
$\langle E_{VC} \rangle$	5.0	8.0	10.6	6.1	11.6	17.5
$\langle E_{SS} \rangle$	1.9	3.0	4.6	2.6	6.1	10.4
$\langle E_{SS+hub} \rangle$	1.3	1.3	1.4	1.4	2.8	4.1

Table 6: Comparison (expressed in percentage) of the axial mean velocity results between those predicted by VC, SS and $SS + hub$ models and PIV velocity measurements, at three selected radial positions: $r = 0$, $r = R/2$ and $r = R$, and its radial average $\langle E \rangle$. At $r = 0$, the comparison is also done using the Vortex Sheet (VS) model (Eq. 5).

plane was shown to be mainly governed by the turbine rotational speed. Even if the deceleration decreases with the thrust coefficient, the overall shape of the mean axial velocity profiles remained unchanged in the proximity of the rotor: the uniform flow evolved to a shear flow with a peak velocity deficit in front of the hub. The mean radial velocity component was not sensitive to the turbine rotational speed in front of the hub, while its values increased near the blade tip as the TSR increases. Second-order statistical analysis shown that the kinetic energy is redistributed near the rotor as a result of the turbine rotational speed. The level of the axial normal component of the Reynolds stress tensor $\overline{u'^2}$ remained globally the same regardless of the TSR: it increased in front of the hub and decreases along the radial direction. In contrast, the level of the radial component $\overline{u_r'^2}$ increased along the radial direction as the TSR increases. The values of the third- and fourth-order velocity statistics differed in front of the operating turbine when compared with those in free flow, confirming that the rotating blades modify the incoming flow intermittency. However, given the TSR values under consideration in this study, no clear impact of the TSR on the skewness and flatness coefficients was highlighted.

In this work, we also investigated the validity of selected analytical models dedicated to estimating the mean axial velocity deficit in front of the turbine. The use of the simple expression of the velocity deficit along the rotor axis, as given by the axial momentum theory, has shown some limitations, especially

close to the hub. The Vortex and Self-Similar models can not reproduce the flow deficit in front of an operating turbine. It was then demonstrated that, to improve the analytical induction model, it was necessary to distinguish between the induction related to the hub cone from the one related to the rotating blades. In this sense, we proposed a new turbine induction model that accounts for the effects of both the hub and the rotating blades, separately. The Self-Similar model based on the associated rotating blade thrust coefficient was then coupled to the hub model characterizing the velocity deficit in front of an ellipsoidal hub. When comparing the mean axial velocity measurements with the estimates of the $SS + hub$ model, an excellent agreement was found, regardless of the rotational speed of the turbine.

As previously noted, the nacelle plays an important role in the development of the turbine near the wake (Kang et al., 2014; Abraham et al., 2019), and the hub vortex behind the nacelle influences the wake meandering (Kang et al., 2014). We then demonstrated that taking into account the hub separately in the analytical turbine induction model significantly improves the description of the mean flow deficit in front of an operating turbine. This could have some implications in Blade Element Method (BEM) methods for accessing the incoming velocity in front of the blades and the hub.

The flow modifications close to the rotor were analyzed and compared well with analytical models in the case of a low disturbance uniform flow for three TSRs around the nominal functioning point. In a future work, it is essential to extend this analysis: i) to incoming shear mean flow conditions and ii) to higher turbulence level intensity.

Furthermore, future three-dimensional measurements or realistic three-dimensional numerical simulations are recommended to further elucidate the redistribution of kinetic energy in front of the turbine. This certainly has a noticeable impact on the fatigue of the blade structure.

CRediT authorship contribution statement

Lucien Jouenne: Software, Data analysis. **Philippe Druault:** Data analysis, Writing original draft, Writing review & editing. **Jean- Franois Krawczynski:** Data analysis, Writing review & editing. **Grgory Germain:** Conceptualization, Funding acquisition, Writing review & editing.

Declaration of competing interest

The authors declare that they have no known competing financial interests or personal relationships that could have appeared to influence the work reported in this paper.

Data availability

Data will be made available on request.

Acknowledgments

This research was partly funded by the European Commission H2020 Programme for Research & Innovation RealTide Project, grant number 727689, and by the Region Hauts-de-France, France in the framework of the project CPER 20152020 MARCO. The authors would like to gratefully acknowledge Benoît Gaurier and Maria Ikhennicheu involved in the experimental database generation and to warmly thank Thomas Bacchetti and Jean-Valery Facq for their assistance and precious advices.

References

Abraham, A., Dasari, T., Hong, J., 2019. Effect of turbine nacelle and tower on the near wake of a utility-scale wind turbine. J. Wind Eng. Ind. Aerodynamics 193, 103981.

Adcok, T., Draper, S., Willden, R., Vogel, C., 2020. The fluid mechanics of tidal stream energy conversion. Annu. Rev. Fluid Mech. 53, 287–310.

Anderson, B., Branlard, E., Vijayakumar, G., Johnson, N., 2020. Investigation of the nacelle blockage effect for a downwind turbine. J. Phys.: Conf. Series 1618 (062062).

Bangga, G., Lutz, T., Jost, E., Krämer, E., 2017. CFD studies on rotational augmentation at the inboard sections of a 10 mw wind turbine rotor. J. Renew. Sustainable Energy 9 (2), 023304.

Bastankhah, M., Porte-Agel, F., 2017. Wind tunnel study of the wind turbine interaction with a boundary-layer flow: Upwind region, turbine performance, and wake region. Phys. Fluids 29, 065105.

Blackmore, T., Myers, L., Bahaj, A., 2016. Effects of turbulence on tidal turbines: Implications to performance, blade loads and condition monitoring. Int. Journal of Marine Energy 14, 1–26.

Bontempo, R., Manna, M., 2019. A ring-vortex actuator disk method for wind turbines including hub effects. Energy Conversion and Management 195, 672–681.

Branlard, E., 2017. Wind turbine aerodynamics and vorticity-based methods: Fundamentals and recent application. Springer

Branlard, E., Gaunaa, M., 2015. Cylindrical vortex wake model: right cylinder. Wind Energy 18, 1973–1987.

Branlard, E., Meyer Forsting, A., 2020. Assessing the blockage effect of wind turbines and wind farms using an analytical vortex model. Wind Energy 23, 2068–2086.

Branlard, E., Quon, E., Meyer Forsting, A.Forsting, A., King, J., Moriarty, P., 2020. Wind farm blockage effects: comparison of different engineering models. J. Phys.: Conf. Series 1618 (6), 062036.

Chen, T., Liou, L., 2011. Blockage corrections in wind tunnel tests of small horizontal-axis wind turbines. Exp. Thermal Fluid Science 35 (3), 565–569.

Deskos, G., Payne, G.S., Gaurier, B., Graham, M., 2020. On the spectral behaviour of the turbulence-driven power fluctuations of horizontal-axis turbines. J. Fluid Mech. 904, A13.

Druault, P., Gaurier, B., Germain, G., 2022. Spatial integration effect on velocity spectrum: Towards an interpretation of the $-11/3$ power law observed in the spectra of turbine outputs. Renew. Energy 181, 1062–1080.

Druault, P., Germain, G., 2022. Experimental investigation of the upstream turbulent flow modifications in front of a scaled tidal turbine. Renew. Energy 196, 1204–1217.

Ebdon, T., 2019. The Impact of Turbulence and Turbine Operating Condition on the Wakes of Tidal Turbines. PhD. Thesis. Cardiff University.

García Regodeseves, P., Santolaria Morros, C., 2021. Numerical study on the aerodynamics of an experimental wind turbine: Influence of nacelle and tower on the blades and near-wake. Energy Conversion and Management 237, 114110.

Gaurier, B., Druault, P., Ikhennicheu, M., Germain, G., 2020a. Experimental analysis of the shear flow effect on tidal turbine blade root force from three-dimensional mean flow reconstruction. Philosophical Transactions of the Royal Society A: Mathematical, Physical and Engineering Sciences 378.

Gaurier, B., Ikhennicheu, M., Germain, G., Druault, P., 2020b. Experimental study of bathymetry generated turbulence on tidal turbine behaviour. Renew. Energy 156, 1158–1170.

Gaurier, B., Germain, G., Facq, J.-V., 2017. Experimental study of the Marine Current Turbine behaviour submitted to macro-particle impacts. In: 12th European Wave and Tidal Energy Conference. Cork, Ireland.

Gaurier, B., Ordonez-Sanchez, S., Facq, JV., Germain, G., Johnstone, C., Martinez, R., Salvatore, F., Santic, I., Davey, T., Old, C., Sellar, B., 2020b. MaRINET2 Tidal Energy Round Robin Tests-Performance Comparison of a Horizontal Axis Turbine Subjected to Combined Wave and Current Conditions. J. Mar. Sci. Eng 8 (6), 463.

Glauert, H., 1935. Aerodynamic theory. Springer (Berlin).

Hancock, P., Pascheke, F., 2014. Wind-tunnel simulation of the wake of a large wind turbine in a stable boundary layer: Part 2, the wake flow. Boundary Layer Meteo. 151 (1), 23–37.

Howard, K., Guala, M., 2015. Upwind preview to a horizontal axis wind turbine: a wind tunnel and field-scale study. Wind Energy 19, 1371–1389.

Ikhennicheu, M., 2019. Étude expérimentale de la turbulence dans les zones à forts courants et de son impact sur les hydroliennes. Ph.D. thesis, Université de Lille.

Ikhennicheu, M., Germain, G., Druault, P., Gaurier, B., 2019a. Experimental investigation of the turbulent wake past real seabed elements for velocity variations characterization in the water column. Int. J. Heat Fluid Flow 78, 108426.

Ikhennicheu, M., Germain, G., Druault, P., Gaurier, B., 2019b. Experimental study of coherent flow structures past a wall-mounted square cylinder. Ocean Eng. 182, 137–146.

Ikhennicheu, M., Germain, G., Gaurier, B., 2019c. Experimental database of a tidal turbine in a wall-mounted square cylinder wake. SEANOE . https://doi.org/10.17882/62635.

Ikhennicheu, M., Germain, G., Gaurier, B., 2019d. Experimental database of the flow past a wall-mounted square cylinder. SEANOE . https://doi.org/10.17882/59027.

Ishihara, T., Qian G.W., 2018. A new Gaussian-based analytical wake model for wind turbines considering ambient turbulence intensities and thrust coefficient effects. J. Wind Eng. Ind. Aerodynamics 177, 275–292.

Joukowsky, N., 1912. Vortex theory of screw propeller. Trudy Otdeleniya Fizicheskikh Nauk Obshchestva Lubitelei Estestvoznaniya (In Russia) 16 (1), 1–31.

Kang, S., Yang, X., Sotiropoulos, F., 2014. On the onset of wake meandering for an axial flow turbine in a turbulent open channel flow. J. Fluid Mech. 744, 376–403.

Kidambi Sekar, A., van Dooren, M., Rott, A., Kühn, M., 2021. Modelling the wind turbine inflow with a reduced order model based on spinnerlidar measurements. Wind Energy Science Discussions, 1–26.

Kolekar, N., Banerjee, A., 2015. Performance characterization and placement of a marine hydrokinetic turbine in a tidal channel under boundary proximity and blockage effects. Appl. Energy 148, 121–133.

Kolekar, N., Vinod, A., Banerjee, A., 2019. On blockage effects for a tidal turbine in free surface proximity. Energies 12 (17), 3325.

Li, C., Abraham, A., Li, B., Hong, J., 2020. Incoming flow measurements of a utility-scale wind turbine using super-large-scale particle image velocimetry. J. Wind Eng. Ind. Aerod. 197, 104074.

Magnier, M., Druault, P., Gaurier, B., Germain, G., 2020. Comparison of bathymetry variation effects on tidal turbine behaviour. In: 17èmes journées de l'hydrodynamique. Cherbourg, France.

Magnier, M., Druault, P., Germain, G., 2021. Experimental investigation of upstream cube effects on the wake of a wall-mounted cylinder: Wake rising reduction, tke budget and flow organization. Eur. J. Mech. B/Fluids 87, 92–102.

Mann, J., Pena, A., Troldborg, N., Andersen, S., 2018. How does turbulence change approaching a rotor? Wind Energy Science 3, 293–300.

Martinez, R., Gaurier, B., Ordonez-Sanchez, S., Facq, JV. Germain, G., Johnstone, C., Santic, I., Salvatore, F., Davey, T., Old, C. Sellar, BG., 2021. Tidal Energy Round Robin Tests: A Comparison of Flow Measurements and Turbine Loading. J. Mar. Sci. Eng. 9(4), 425.

Medici, D., Ivanell, S., Dahlberg, J.-Å., Alfredsson, P. H., jul 2011. The upstream flow of a wind turbine: blockage effect. Wind Energy 14 (5), 691–697.

Meyer Forsting, A., Bechmann, A., Troldborg, N., 2016. A numerical study on the flow upstream of a wind turbine in complex terrain. J. Phys.: Conf. Series 753, 032041.

Meyer Forsting, A., Van der Laan, M., Troldborg, N., 2018. The induction zone/factor and sheared inflow: A linear connection ? J. Phys.: Conf. Series 1037, 072031.

Milne, I.A., Graham, J.M.R. 2019. Turbulence velocity spectra and intensities in the inflow of a turbine rotor J. Fluid Mech. 870, R3.

Mycek, P., Gaurier, B., Germain, G., Pinon, G., Rivoalen, E., 2014. Experimental study of the turbulence intensity effects on marine current turbines behaviour. Part I: One single turbine. Renew. Energy 66, 729–746.

Mycek, P., Gaurier, B., Germain, G., Pinon, G., Rivoalen, E., 2014. Experimental study of the turbulence intensity effects on marine current turbines behaviour. Part II: Two interacting turbines. Renew. Energy 68, 876–892.

Schreck, S., Robinson, M., 2022. Rotational augmentation of horizontal axis wind turbine blade aerodynamic response. Wind Energy 5 (2-3), 133–150.

Segalini, A., 2021. An analytical model of wind-farm blockage. J. Renew. Sustainable Energy 13 (033307).

Sentchev, A., Thiébot, J., P. M., Bennis, A., 2020. Theme Issue: New insights on tidal dynamics and tidal energy harvesting in the Alderney Race. Phil. Trans. Royal Society A.

Shoukat, G., Gaurier, B., Facq, J. V., Payne, G. S., 2022. Experimental investigation of the influence of mast proximity on rotor loads for horizontal axis tidal turbines. Renew. Energy 200, 983–995.

Simley, E., Angelou, N., Mikkelsen, T., Sjöholm, M., Mann, J., Pao, L. Y., 2016. Characterization of wind velocities in the upstream induction zone of a wind turbine using scanning continuous-wave lidars. J. Renew. and Sustainable Energy 8 (1).

Slinger, C., Harris, M., Pitter, M., 2020. Wind speed measurement for absolute power curve determination from induction zone lidar measurements. J. Phys.: Conf. Series 1618, 032027.

Sørensen, J., 2016. General Momentum Theory for Horizontal Axis Wind Turbines. Springer.

Troldborg, N., Meyer Forsting, A., 2017. A simple model of the wind turbine induction zone derived from numerical simulations. Wind Energy 20, 2011–2020.

Van Kuik, G., Peinke, J., Nijssen, R., Lekou, D., Mann, J., Sørensen, J., Ferreira, C., van Wingerden, J., Schlipf, D., Gebraad, P., et al., 2016. Long-term research challenges in wind energy–a research agenda by the european academy of wind energy. Wind energy science 1 (1), 1–39.